Extrusion-Based Printing of Nanostructured Fatty Acid Gels Incorporated in Hydrogels

Saba Amirfattahi[1], Cody J. Freeman[1], Houman Honaryar[1], Hanieh Sadat Ghazali[1], Kyungtae Kim[2], and Zahra Niroobakhsh[1,→]

[1]Division of Energy, Matter, and Systems, School of Science and Engineering, University of Missouri-Kansas City, Kansas City, Missouri 64110, USA.

[2]Materials Physics and Applications Division, Center for Integrated Nanotechnologies, Los Alamos National Laboratory, Los Alamos, New Mexico 87545, USA.

E-mail: Niroobakhshz@umkc.edu

Abstract

Soft materials with unique nanostructures, such as lamellar, hexagonal, and cubic morphologies, can replicate complex structures that have potential in various fields including biomedical and industrial applications. However, a key challenge in advancing the broader applications in 3D printing for these nanostructured soft materials is insufficient mechanical properties that hinder their printability and compromise structural stability in the final product. In this study, the suitability of a fatty acid-based lamellar gel is evaluated for direct extrusion-based 3D printing. The lamellar gel with varying water content is integrated with a photocurable hydrogel to preserve the shape and stability of the final prints. Complex 2D and 3D design patterns are used to assess extrusion behavior, structural stability, and print precision under varying pressures. Small-angle X-ray Scattering (SAXS) measurements reveal the formation of lamellar nanostructures and confirm their retention after photocuring in various gels. Rheological analysis confirms that these gels exhibit key properties suitable for extrusion-based

3D printing, such as shear-thinning behavior. Additionally, tensile testing is conducted to evaluate the mechanical properties across cured print samples. This study underscores the potential of nanostructured gels as a robust and versatile platform, facilitating the development of materials engineered for various applications.

Introduction

Having stable, nanostructured soft materials can be beneficial in various fields, such as food and cosmetic industries, as well as biomedical and pharmaceutical applications.[1–11] However, printing and structuring soft materials into 3D constructs is challenging due to their low mechanical strength and limited stability.[12–14] Despite these limitations, their ability to mimic the complexity of biological tissues—featuring hierarchical organization, self-healing, and perfusion[15,16]—enhances their potential for diverse applications. Incorporating specific nanostructures, such as lamellar[17,18] and hexagonal[19,20] phases, significantly improves their mechanical stability and functionality, making them more e!ective than liquid-like counterparts.

The primary approach for printing soft materials has been layer-by-layer deposition, where the printing phase is placed onto a print bed or preceding layers to form the final construct.[21–23] These techniques, also referred to as direct extrusion 3D printing or direct ink writing, are cost-e!ective, minimize waste, simplify processing, and allow multiple inks within the same construct.[14,24–32] Direct extrusion-based 3D printing is particularly e!ective for materials with high shear-thinning behavior, where viscosity decreases under the shear stress. Additionally, advanced rheological optimization strategies enhance control over flow behavior and address the deformation challenges. These properties are essential for maintaining structural fidelity during and after printing.[33–35]

Direct extrusion 3D printing techniques support a wide range of soft materials, such as colloidal gels,[36–41] polymeric gels,[42,43] and hydrogels,[22,44–49] each presenting unique benefits and limitations. Recent research into nanostructured soft materials composed primarily

of surfactants, water, and oils has shown promising potential for 3D printing, particularly when using oils with headgroup polarity, such as fatty acids and fatty alcohols.[50,51] These oils serve dual roles as both an oil phase and a co-surfactant, adding versatility to the ternary system.[13,52,53] Their natural abundance, biocompatibility, and low toxicity make these systems appealing for biotechnological applications, including bioprinting.[52,54–58] Their highly ordered nanostructural arrangements also o!er tunable and unique rheological properties such as shear-thinning behavior, providing precise mechanical control that is critical for applications such as extrusion-based 3D printing and bioprinting.[59]

Previous studies have demonstrated the potential of fatty acid-based gels with well-defined nanostructural properties, particularly in self-assembled surfactant systems.[13,53] However, they lack a robust fabrication method to shape these gels into complex geometries, limiting their practical applications. Prior approaches, such as the associative liquid-in-liquid 3D printing platform, enabled the in situ production of nanostructured gel materials by printing aqueous surfactant solutions into an oil bath.[50,54,60] While e!ective, this method relies on a bath medium, requiring additional post-processing steps for print retrieval and washing. To overcome these limitations, this study introduces a direct extrusion-based 3D printing platform that eliminates the need for a printing bath, simplifying fabrication and preserving nanostructural integrity.[14,54]

This study introduces a novel integration of a lamellar gel—formed from a ternary system of surfactant, fatty acid, and water—into a hydrogel matrix for enhanced structural stability. The gels consist of oleic acid (OA) as the oil phase, cetylpyridinium chloride (CPCl), water, polyethylene glycol diacrylate (PEGDA) as the hydrogel component, and 1-hydroxycyclohexyl phenyl ketone (HCPK) as the photoinitiator. PEGDA and HCPK are considered part of the aqueous phase, maintaining an equimolar surfactant/oil composition (Figure 1A) with varying water content: high (sample E4), intermediate (sample E5), and low (sample E6). By incorporating the hydrogel directly during gel preparation, this approach preserves the equimolar composition while o!ering a structurally reinforced system

compared to previous formulations.[13]

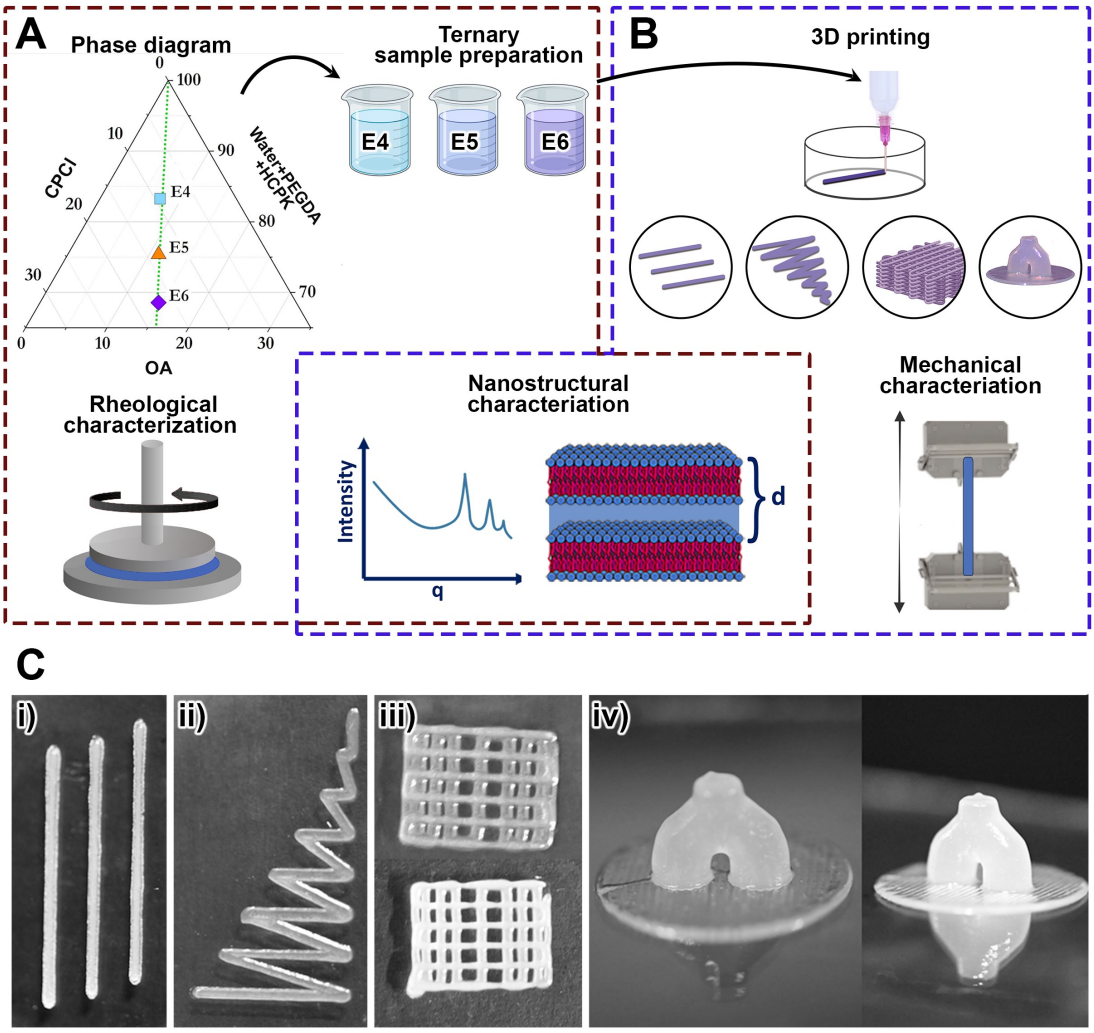

Figure 1: (A) Pseudo-ternary phase diagram and the composition of studied samples (along the equimolar OA/CPCl line, represented by the dashed line). Nanostructural and rheological characterization were carried out on the prepared pseudo-ternary gel samples using small angle X-Ray scattering and shear rheometry. (B) The prepared gel samples are 3D printed into various designs and subsequently characterized for their nanostructure and mechanical properties. (C) Representative images of printed structures with various designs using the gel samples referred to as: (i) straight lines, (ii) serrated pattern for edge and angle precision, (iii) bridging geometry for self-supporting capability, and (iv) 3D bifurcating structure for structural complexity assessment.

Various designs were employed to assess the printability of the samples (Figure 1B) and optimize printing parameters for complex three-dimensional structures. These designs

ranged from simple 2D straight lines (Figure 1C-i) to evaluate extrusion consistency, to serrated patterns (Figure 1C-ii) for testing edge definition, bridging geometries (Figure 1C-iii) for self-supporting properties, and bifurcating structures (Figure 1C-iv) for assessing structural complexity. SAXS measurements confirmed the preservation of lamellar morphology in both uncured gels and printed fibers, with enhanced lamellar order after curing. Rheological analysis revealed significant shear-thinning behavior, facilitating smooth extrusion, with the storage modulus ($G^{\rightarrow}$) consistently exceeding the loss modulus ($G^{\rightarrow\rightarrow}$) across all angular frequencies. Among the tested samples, E6 exhibited the highest mechanical strength, while E4 had the lowest, corresponding to their respective water contents. Additionally, tensile testing of the cured samples demonstrated improved mechanical strength compared to their soft gel state, highlighting the e!ectiveness of hydrogel integration in reinforcing structural stability.

Results

3D Printing

For printing of the gels, three di!erent compositions were chosen on the equimolar line of CPCl surfactant and OA oil, including E4, E5, and E6 samples (Figure 1A). During sample preparation, hydrogel (PEGDA) and photoinitiator (HCPK) were added to water to achieve a PEGDA concentration of 30 wt/vol% in the aqueous phase, with HCPK constituting 5 wt% relative to the hydrogel weight. The detailed composition of these gels can be found in Table 2.

As for the printing parameters, the extrusion pressure is varied while the nozzle size of 25G and printing speed of 10 mm $s^{\uparrow 1}$ remain constant. During the printing and upon contact of the gels with the printing surface, self-supporting materials maintained their shape, and then the printed construct was cured after a 10-second of exposure to UV light.

The printability and structural stability of gel samples (E4, E5, and E6) were evalu-

ated across progressively complex geometries, referred to as straight lines, serrated patterns, bridging designs, and 3D bifuricating structures, as shown in Figure1C and Figure S1-S3(Supporting Information).

Straight lines are used to evaluate structural stability during printing and curing, determining critical printability parameters such as the extrusion rate. Serrated patterns, characterized by sharp, angular peaks and valleys, are employed to assess edge and angle precision, with a focus on pressure control at corners and deflections. The third design, known as bridging geometry, features a 3D sca!old-like structure designed to test self-supporting capabilities across unsupported spans. The most intricate design, referred to as 3D bifurcating structures, is printed to examine the ability to handle structural complexity.

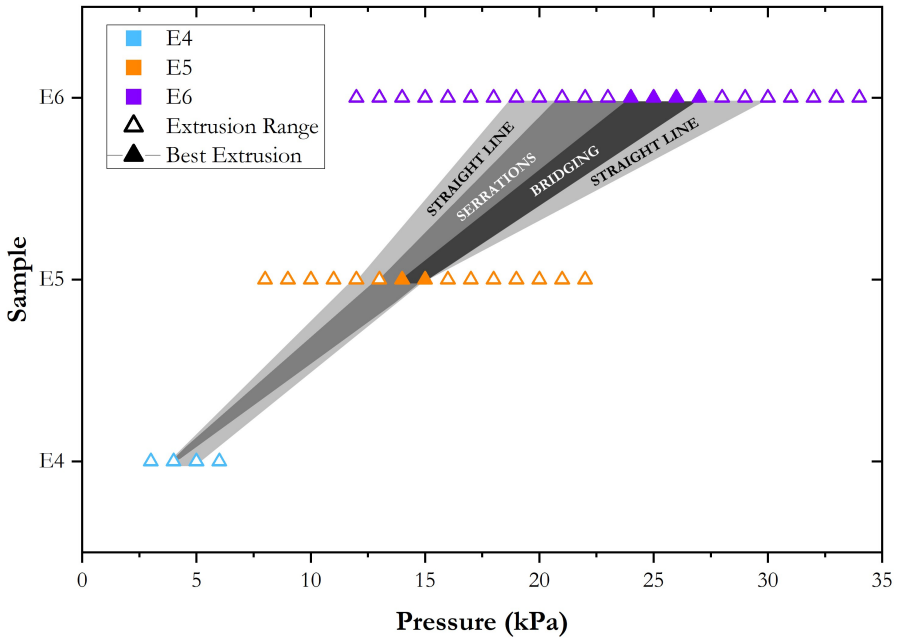

Figure 2: Examined extrusion pressure for E4, E5, and E6 samples represented by triangles. Filled triangles represent the optimal, workable extrusion pressure for specific geometries, with shaded regions for each test geometry to guide the eyes.

Figures S1–S3 (Supporting Information) summarize the key findings, highlighting the relationship between extrusion pressure, viscosity of gels, and print quality. Optimal pressure ranges were determined for each geometry and material, with E5 and E6 outperforming E4

due to their higher viscosities and broader pressure windows. The ideal pressure ranges for each sample across di!erent evaluation geometries have been determined and presented in Figure 2. The unfilled triangle points before and after the shaded regions represent tested pressures where extrusion occurred but with either under-extrusion or significant over-extrusion.

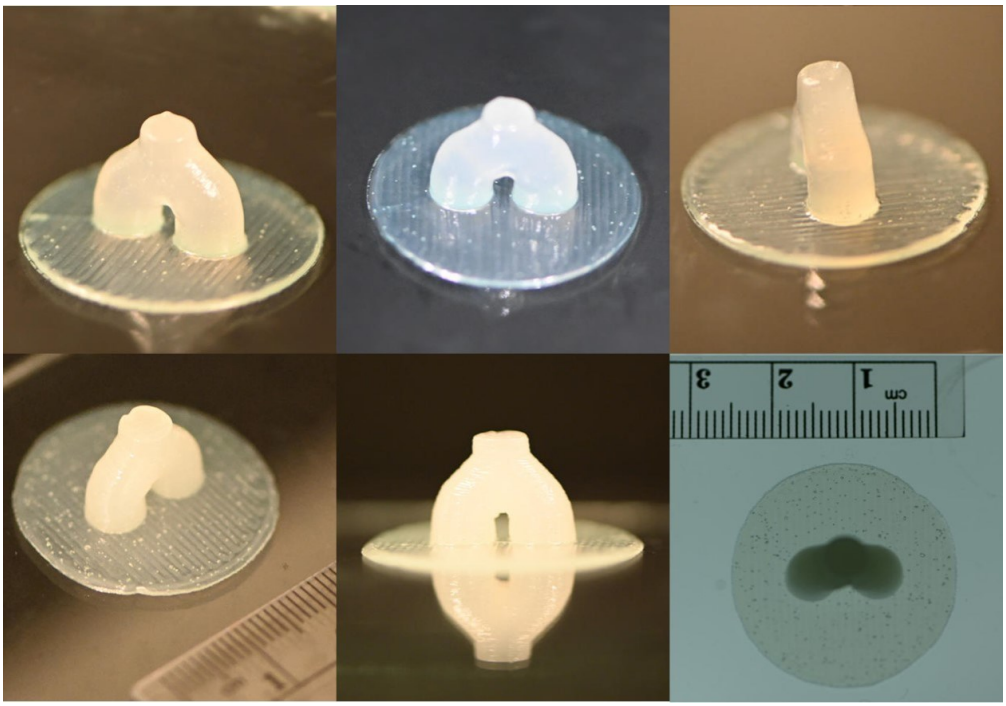

Figure 3: Demonstration of bifurcating structure 3D printed with sample E5 at the top row and sample E6 at the bottom row.

The filled triangles and darkest shaded region, labeled "BRIDGING," represent the precise extrusion pressure range for samples E4, E5, and E6, where the ideal amount of material is deposited for the bridging geometry, and the ideal prints were achieved. Building on a foundational understanding of optimal printing pressures for various geometric designs, a more complex three-dimensional bifurcating structure was tested. For printing conditions, the extrusion pressure was selected from the optimal "BRIDGING" conditions to further evaluate the gel performance in handling structural complexity. For these samples, the structures were fully printed and then subjected to 30 seconds of UV curing post-printing. Examples of 3D printed bifurcating structures for E5 and E6 are shown in the top and bot-

tom rows of Figure 3. Each sample was evaluated despite sample E4 being excluded from the previous bridging geometry test. As anticipated, sample E4 encountered issues early on, failing to produce a complete print. By the second layer, sample E4 could not maintain a defined structure and spread into a puddle, prompting the termination of the print. Unlike sample E4, samples E5 and E6 consistently exhibited stability and structural accuracy, producing self-supporting 3D structures across multiple trials. Notably, sample E6 exhibited more distinct layer lines, o!ering a clearer visualization of the layered print structure. In contrast, sample E5 showed slight flow during printing, which smoothed out the layer lines and reduced fidelity at sharper transitions, giving the structure a smoother appearance.

Small Angle X-Ray Scattering (SAXS) Measurements

SAXS measurements were performed on uncured gels and cured printed fibers to characterize their nanostructural properties. Isotropic scattering patterns observed in Figures 4A confirm the presence of lamellar nanostructures in the uncured samples, with a primary domain spacing of ↑ 7 nm following a sequence that aligns with a $\overset{\downarrow}{1}, \overset{\downarrow}{4}$ pattern.[61–63] A secondary anisotropic lamellar sequence with a smaller domain spacing of 5 nm, notated as $\overset{\downarrow}{1}_2$, and $\overset{\downarrow}{4}_2$), consistent with previous studies.[54] The SAXS peaks become sharper and narrower from E4 to E6. This behavior is expected for E4 gel samples, which have a higher water content (82.9 wt%) compared to E5 (75.0 wt%) and E6 (68.5 wt%). The decrease in water content increases the surfactant concentration, reducing the spacing between bilayer sheets and promoting reduced domain spacing in the lamellar structures.[13]

After curing, all samples exhibited a consistent lamellar spacing of 5 nm, with significantly sharper Bragg peaks compared to the uncured gels (Figure 4B). This observation indicates that the curing process enhances the uniformity of the lamellar nanostructure across samples. Notably, the cured E4 fibers displayed the sharpest and narrowest peaks among all samples. Figure 4C summarizes the domain spacing for all samples, while Figure 4D shows the 2D SAXS scattering images, highlighting both primary and secondary lamellar rings.

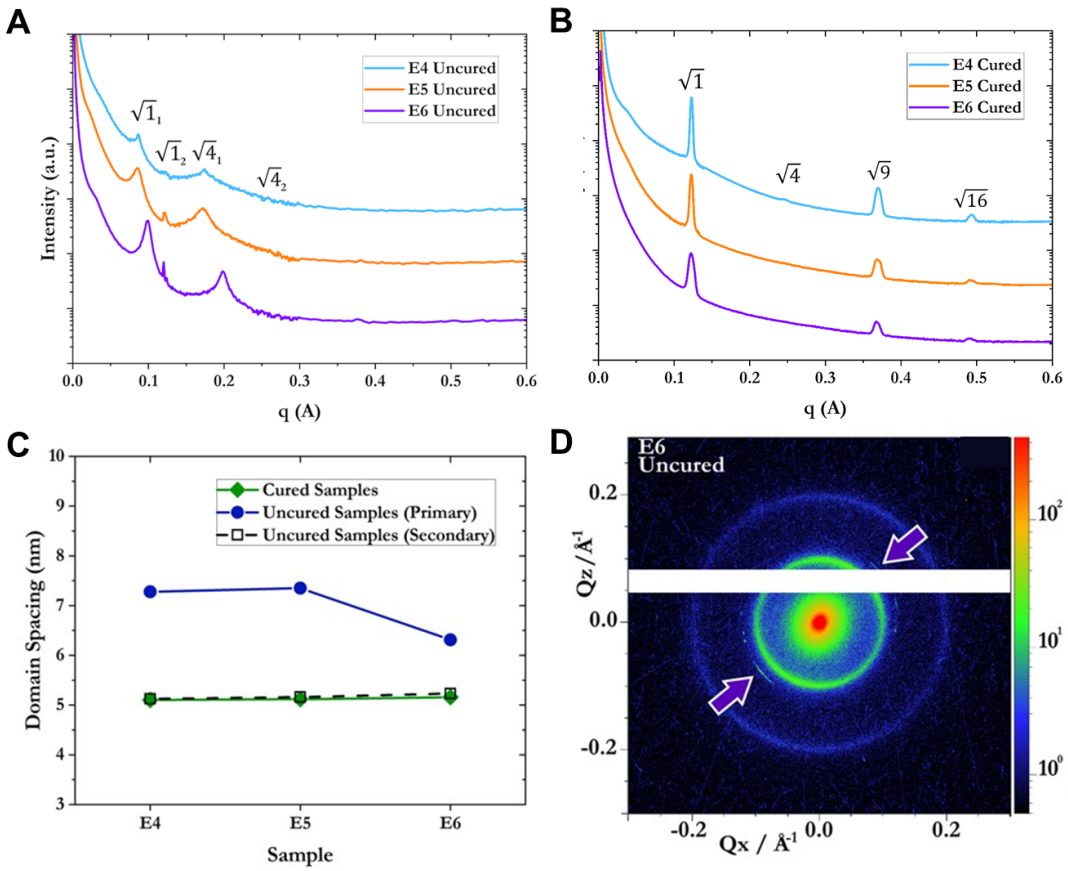

Figure 4: SAXS analysis for the gels and printed fiber samples, illustrating nanostructural organization in both uncured and cured states. Isotropic scattering patterns in linear mode for (A) uncured gels and (B) cured fibers. Scattering profiles are vertically shifted on a log I scale for better visualization. (C) Graph showing the measured domain spacings across various samples. (D) A representative 2D scattering pattern for an uncured samples shows the prominent lamellar ring rep- resenting the primary peaks. A faint secondary lamellar ring is also visible, as indicated by the arrow.

Rheological Measurements

The rheological measurements of the gel sample before printing and curing were performed. For the frequency sweep results, the storage ($G^{\rightarrow}$) and loss ($G^{\rightarrow\rightarrow}$) moduli remain largely inde- pendent of angular frequency for all examined samples, as shown in Figure 5A. Each sample displays a roughly one order of magnitude di!erence between $G^{\rightarrow}$ and $G^{\rightarrow\rightarrow}$, with storage moduli exceeding loss moduli. This behavior indicates typical viscoelastic behavior. As shown in Figure 5B, the average storage moduli for samples E4 and E6 are the lowest and highest,

respectively. Additionally, Figure 5C shows that all samples exhibit shear-thinning behavior, with viscosity decreasing nearly linearly by approximately 2.5 to 3.5 orders of magnitude as shear rates increase. Furthermore, sample E5 has a higher viscosity than sample E6, in contrast with the storage moduli described for Figure 5B. This increase in moduli is expected due to reduced water content in their compositions.

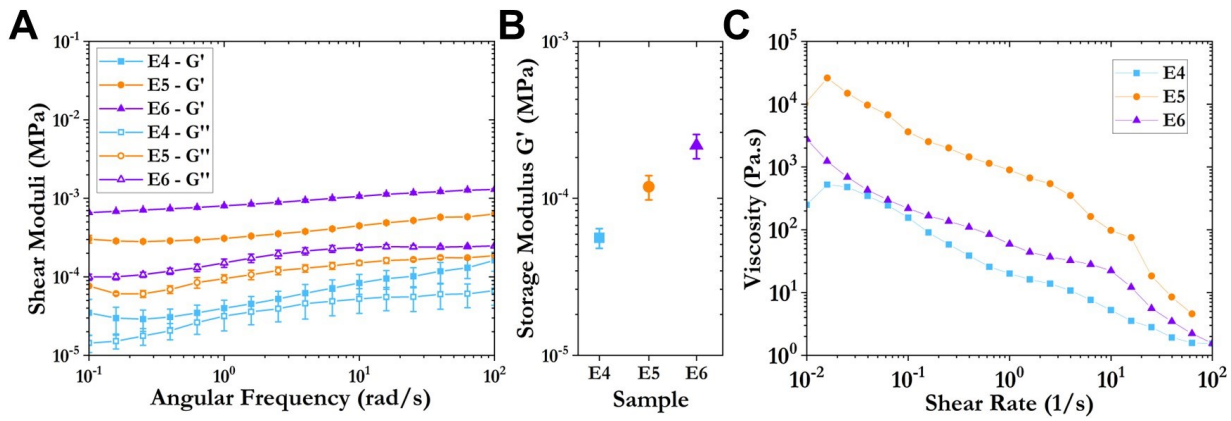

Figure 5: Rheological characterization for samples of E4, E5, and E6. (A) Storage [$G^{\rightarrow}$] and loss [$G^{\rightarrow\rightarrow}$] moduli with standard error over a range of angular frequencies. (B) Average storage moduli [$G^{\rightarrow}$] for samples E4, E5, and E6 across their full range of angular frequencies. (C) Viscosity as a function of shear rate exhibiting favorable shear thinning behavior.

To measure yield stress, stress (ω) vs. shear rate ($\dot{\varepsilon}$) data were fitted to the Herschel–Bulkley model (Figure S4 A, B, and C (Supporting Information)). Yield stress formula from the Herschel–Bulkley model formula is: $\omega=\omega_y+K\dot{\varepsilon}^n$ where ω is shear stress, ω_y is the yield stress, K is Consistency index, and n is flow index. The model was applied to steady-state data, ensuring the sample remained intact at high shear rates. In all cases, the Herschel-Bulkley model showed a significant fitting to experimental data ($R^2 > 0.95$). The resulting yield stress and other rheological properties values for all three samples are reported in Table 1. The results suggest that sample E5 shows the highest yield stress, which is consistent with its highest modulus. All of the three samples showed shear thinning behavior with $n<1$.

Table 1: Summary of rheological properties of samples.

Sample	Yield Stress (Pa)	K(Pa.s^n)	n	R^2	Viscosity$^{\downarrow}$ (Pa.s)
E4	13.005	9.258	0.57021	0.9673	20.0631
E5	271.571	579.879	0.54375	0.9588	894.442
E6	13.151	46.472	0.65973	0.9952	59.1854

$^{\downarrow}$The viscosity values are reported at the shear rate of 1 $s^{\uparrow 1}$.

Mechanical Evaluation

Mechanical properties of the printed fibers were evaluated using tensile testing. Due to its fragility, sample E4 was excluded from mechanical testing. Representative stress-strain curves for samples E5 and E6 are shown in Figure 6B, with key mechanical parameters—Young's modulus, tensile strength, and elongation at break—summarized in Figures 6C-E.

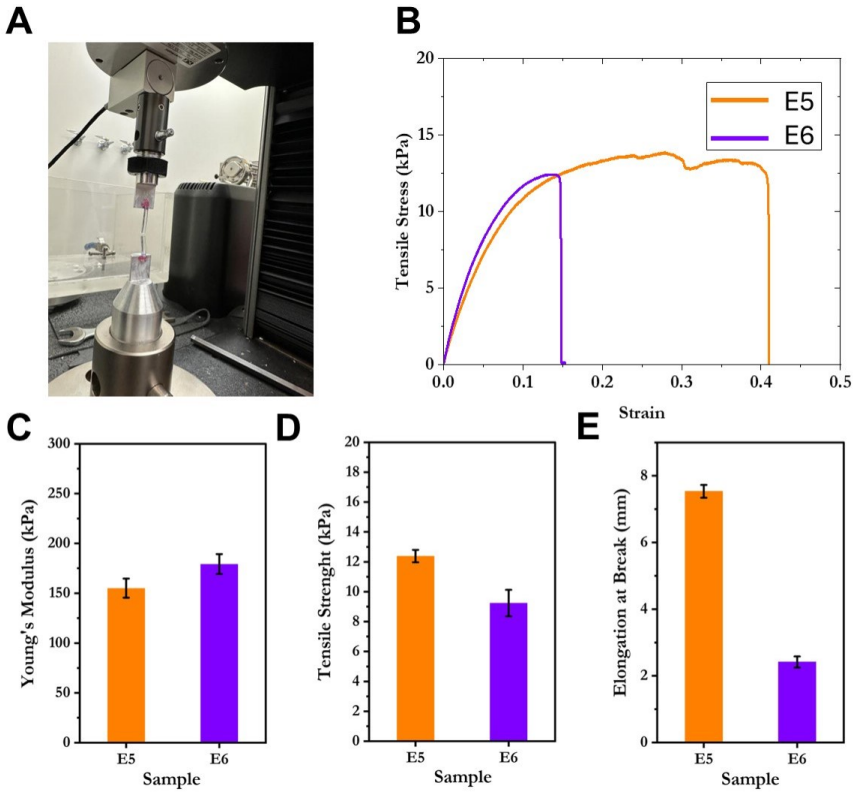

Figure 6: (A) Mechanical testing load cell with representative failed tensile sample. (B) representative Stress-Strain plot for specimen produced from each of samples E5 and E6. The averaged values are shown in (C) for Young's moduli, (D) for tensile strength, and (E) for elongation at break for samples E5 and E6.

Both samples exhibited similar Young's moduli, measured at ↔155±9 kPa for sample E5 and ↔179±10 kPa for sample E6 (Figure 6C). Tensile strength was slightly higher for sample E5 (↔12±0.5 kPa) compared to E6 (↔9±1 kPa) (Figure 6D). In contrast, elongation at break was significantly greater for sample E5 (↔7±0.2 mm) compared to E6 (↔2.4±0.2 mm) (Figure 6E), suggesting that E6 fibers were more brittle and less ductile. Additionally, sample E6 exhibited stronger adhesion to the printing surface, which may have influenced mechanical test results due to potential structural damage during removal.

Discussion

This study investigates the suitability of a nanostructured gel material for extrusion-based printing. The gel systems comprise a fatty acid oil (oleic acid), a surfactant (CPCl), and water incorporated in a hydrogel (PEGDA). The gels were printed into various geometries using extrusion-based printing, followed by UV curing. The extrusion pressure was varied to assess the printability of the gels. To evaluate extrusion pressure performance and print fidelity, designs of increasing complexity were used, progressing from simple lines to serrations, bridging, and eventually to 3D bifurcating structures. As the geometries became more complex, the workable extrusion pressure range narrowed due to challenges such as under-extrusion and over-extrusion in areas with kinks and nooks.

As anticipated, gels with higher viscosities (lower water content) required higher extrusion pressures. The sample with the highest water content (E4) exhibited a narrow extrusion pressure window and struggled to maintain shape fidelity due to its softness, making it suitable only for simpler designs. In contrast, more compact gels with lower water content demonstrated superior performance, accurately printing complex geometries such as serrations, bridging, and 3D bifurcating structures with excellent shape retention. As print complexity increased, the acceptable extrusion pressure range narrowed—for example, while straight-line printing covered the entire shaded range, more intricate structures like serra-

tions and bridging required more precise pressure control. Notably, reducing water content broadened the acceptable pressure range, minimizing the need for precise adjustments and enhancing the margin for error in direct extrusion 3D printing. These results emphasize the reliability of E5 and E6 for complex, unsupported geometries, with E6 demonstrating enhanced layer distinction and E5 o!ering a smoother, more integrated print surface. Overall, these robust gels show the greatest promise for extrusion-based applications.

The SAXS results demonstrate that incorporating hydrogel into the lamellar ternary gels preserves the lamellar structure while modifying domain spacing and ordering behavior. The observed sharpening of SAXS peaks from E4 to E6 in the uncured gels corresponds to increasing surfactant concentration and lowering water content, reducing bilayer spacing and enhancing structural order. Upon curing, the lamellar structure shrinks to a uniform 5 nm spacing across all samples, aligning with the secondary structure observed in the uncured state.

The observations reveal that the Bragg peaks significantly sharpen post-curing, suggesting a more uniform and tightly packed arrangement. Notably, E4, which initially had the highest water content, exhibited the sharpest peaks post-curing, reversing the trend seen in uncured gels. This suggests that softer gels may facilitate better molecular rearrangement during photopolymerization, contributing to improved structural ordering. These findings align with previous studies on fatty acid-based gels combined with hydrogels, where lamellar nanostructures were observed, but with larger domain spacings (14–29 nm) in hydrogel-free systems.[13,54] The ability to retain lamellar structures while achieving finer, more uniform nanostructures post-curing highlights the potential of these gels for applications requiring precise nanostructural control.

Rheological measurements highlighted the distinct viscoelastic properties of the samples, with all exhibiting a storage modulus ($G^{\rightarrow}$) significantly higher than the loss modulus ($G^{\rightarrow\rightarrow}$), confirming solid-like viscoelastic behavior. As expected, sample E4, with the highest water content, demonstrated the lowest moduli and viscosity, while sample E6, with the lowest

water content, exhibited the highest moduli.This reversed behavior is consistent with previous findings for the same compositions without the hydrogels.[13,48] Interestingly, sample E5 presented the highest viscosity despite its intermediate water content, consistent with previous findings.[13] These rheological properties directly influenced extrusion behavior, where all samples exhibited shear-thinning, facilitating smooth extrusion and deposition. However, the low viscosity and weak shear moduli of sample E4 compromised its ability to recover strength after deposition, reducing print resolution and shape fidelity. Yield stress, critical for maintaining structural integrity post-extrusion, was higher in gels with greater storage modulus, reinforcing sti!ness and form stability.[64,65] Overall, the rheological characteristics of E5 and E6 support their suitability for direct extrusion, particularly for complex and unsupported geometries.

The tensile testing suggests stable mechanical properties for produced cured fibers. The cured fiber of sample E4, which had the highest water content in their gel composition before curing, surprisingly showed the most well-defined structure. However, tensile testing was not feasible due to the samples breaking during handling. The cured fiber of samples E5 and E6, which contains the lower water contents in their compositions compared to sample E4, maintained a Young's moduli ranging from ↔155-180 kPa. A comparison of the cured fibers from samples E5 and E6 indicates reduced ductility in E6. However, this cannot be directly attributed to its inherent ductility due to variations in attachment strength to the printing bed. Tensile testing was not feasible for E4 fiber due to sample breakage during handling. Although it exhibits excellent ordering post-curing, its limited printability and handling challenges constrain its practical applications.

In conclusion, the curing process demonstrated significant improvement in mechanical properties over the uncured gel state, which had poor mechanical stability. Moreover, the lamellar morphology not only preserved but also enhanced its structural uniformity and organization. Furthermore, the type of nanostructure morphology and mechanical properties can be tuned by altering constituent ternary components incorporated in hydrogels. Other

examples of nanostructure-forming ternary systems include combinations of the cationic cetyltrimethylammonium bromide (CTAB), anionic sodium dodecyl sulfate (SDS), or non-ionic Tween 20 or Pluronic F68 surfactants in various oil-based co-surfactants.[50,54] Maintaining nanostructures and ensuring stable mechanical properties are crucial for achieving the desired application. For instance, current system shows the Young's moduli around a few hundred kPa that covers a wide range of mechanical characteristics, including those found in natural human tissues.[1,66–70] This approach enables the diversification of nanostructure morphologies and the customization of mechanical properties within hydrogels, making them suitable for a wide range of applications.

Conclusion

This study demonstrated the potential of nanostructured fatty-acid-based gels combined with hydrogels for extrusion-based 3D printing. It successfully transforms nanostructured gels into high-fidelity complex geometries by introducing varying levels of intricacy in the printing patterns, spanning straight fibers, serrated designs, bridging configurations, and bifurcating structures. The incorporation of hydrogels helped preserve the lamellar nanostructures in the samples after curing. Small-angle X-ray Scattering (SAXS) measurements confirmed an enhancement in nanostructural order following curing. Also, rheological evaluations revealed shear-thinning behavior and solid-like viscoelastic properties for all three samples, which are essential for controlled extrusion. Furthermore, the combined results of SAXS and rheological measurement on uncured gels were aligned with the previous study of the system without hydrogel.[13] Tensile testing displayed enhanced mechanical properties. The combined findings from this study suggest that this material system with preserved nanostructures and desirable mechanical properties holds significant promise for a variety of applications.

Experimental Section

Materials

Oleic acid (OA, technical grade 90%) was obtained from Alfa Aesar. Cetylpyridinium chloride monohydrate (CPCl, 99.0–102.0%), polyethylene glycol diacrylate (PEGDA, average M_n=700 g mol$^{\uparrow 1}$), and 1-hydroxycyclohexyl phenyl ketone (HCPK) photoinitiator were purchased from Sigma-Aldrich. All chemicals were used as received without further purification. Purified, deionized water was used for preparing samples.

Sample Preparation

For preparing samples, the OA and aqueous solution of CPCl were combined along their equimolar line with water, resulting in mixtures ranging from liquid-like to gel-like states as water content was reduced. These compositions are depicted in Figure 1A and detailed in Table 2. For making the samples containing hydrogel and to keep the ratio of CPCl and oleic acid the same, PEGDA was added as a substitute for water, and its concentration was maintained at 30 wt/v% of the aqueous phase. To prepare this mixture, CPCl was dissolved in deionized water and sonicated until a homogeneous, clear solution formed. In a separate vial, HCPK was added to PEGDA at 5 wt/wt% relative to the PEGDA weight and sonicated until all small fragments of HCPK fully dissolved in the PEGDA. After preparing these two solutions, they were combined into a single vial. Finally, oleic acid was added to the resulting mixture. The samples were then manually stirred using a spatula and sonicated, resulting in a slimy texture. It is worth mentioning that our previous study on samples without hydrogels[13] involved stirring and/or shaking the mixture at 40–80°C for several days, followed by 15 minutes of sonication to ensure full dissolution of oleic acid, as elevated temperatures are typically required for similar ternary systems[71–73] but for PEGDA-containing samples in this work, heating was not used to prevent premature polymerization of PEGDA.

Table 2: Summary of compositions used for each system with hydrogel.

Sample	OA (ml)	Water (ml)	CPCl (gr)	PEGDA (ml)	HCPK (gr)
E4	1.5	10	1.613	3.812	0.1067
E5	2.5	10	2.564	3.812	0.1067
E6	3.43	10	3.534	3.812	0.1067

Printing

Each sample was transferred into appropriate UV-resistant 3 ml syringes with single-use plastic spatulas, with care given to reduce entrapped air within the syringe. Each syringe was filled to near full capacity and spun in a centrifuge to remove air bubbles. The centrifuge process generally took only 10-15 seconds at speed for compaction of the material to occur within the syringe but was allowed to run for no less than 30 seconds to de-bubble the samples. Ultimately, some observation of the samples was necessary to evaluate if air pockets had been su"ciently removed. All three samples retained minimal trapped air, with the E6 samples retaining the most.

The CELLINK BIO X6 bioprinter, equipped with a pneumatic head, was used to print the gels. Upon contact with the printing bed, the self-supporting gel maintained its shape. After printing, each construct was cured under UV light for a minute using a copper UV-curing board with four UV LEDs (365 nm, LED Engin), allowing the cured structures to be easily removed from the surface. All three gel compositions were tested, each showing varied results due to di!erences in flow behavior and viscosity. Various print parameter combinations were explored to optimize the print quality, as detailed in Section 3D Printing.

Small Angle X-Ray Scattering (SAXS) Measurements

The small-angle X-ray scattering experiments were carried out using a Xenocs Xeuss 3.0 small-angle/wide-angle X-ray scattering instrument equipped with a Cu Kϑ X-ray source (X-ray wavelength of 1.54 Å and a beam size of 0.4 mm × 0.1 mm) and an Eiger2 R 1M Dectris detector. The sample-to-detector distance was varied from 55 mm to 1650 mm.

The SAXS measurements of cured fiber prints were performed two days after they were fabricated. Until right before the SAXS measurements, the samples were stored in oleic acid. Upon measurements, two-dimensional (2D) scattering patterns were obtained, and azimuthal integration of these scattering patterns resulted in one-dimensional (1D) scattering profiles, I(q), versus scattering vector $q = 4\pi(\sin\theta)\lambda^{-1}$, where θ is the scattering angle and λ is the beam wavelength.

Rheological Measurements

Rheological evaluation of uncured samples was performed on a TA Instruments Discovery-HR3 rheometer at 25 ± 0.5°C. Using parallel plate geometry, about 1.5 ml of each sample was carefully loaded to minimize shear effects, rested for 10 minutes, and set with a 500 µm gap. Amplitude sweep tests (0.01% to 100% strain) at a constant angular frequency of 1 rad/s identified the linear viscoelastic region, followed by oscillatory frequency sweeps (0.1 to 100 rad/s) at 1% strain to obtain storage moduli (G') and loss moduli (G'') values. Sample E4 was tested three times, while E5 and E6 samples were each tested twice. Flow sweep tests were conducted once per sample to measure viscosity changes across a shear rate range of 0.001 to 100 s^{-1}.

Mechanical Properties Characterization

To measure the mechanical properties of each group of printed samples, a minimum of five fiber samples from each composition were printed under consistent conditions, including printing speed, extrusion rate, and temperature. E5 and E6 specimens were printed with no additional nozzle on the syringe, effectively acting as a built-in approximately 2mm nozzle. However, sample E4 had to be printed with a 14G nozzle for extrusion control. The surface area of each fiber was calculated based on dimensions measured with a caliper. The tensile testing was conducted using an Instron 5967 instrument equipped with a 10N load cell (series 2530). Each end of the fiber (with a length of 30 mm) was affixed to the instrument

fixture using Zappit glue (with 5mm from each side overlapping with the fixture, as shown in Figure 6A). Samples were then subjected to uniaxial extension by being steadily stretched at a rate of 0.5 mm $min^{\uparrow 1}$ until they fractured. Young's moduli, elongation at break, and tensile strength were calculated based on the average test results of four samples for E5 and E6 measurements.

Acknowledgment

This work was supported by the 2021 UMKC Faculty for Excellence (UMKC FFE) grant. The funding for this project was partially provided by NSF grant CBET/PMP-2301605. Part of this work was performed at the Center for Integrated Nanotechnologies, an O"ce of Science User Facility operated by the U.S. Department of Energy (DOE) O"ce of Science. Los Alamos National Laboratory, an a"rmative action-equal opportunity employer, is managed by Triad National Security, LLC for the U.S. Department of Energy's NNSA, under contract 89233218CNA000001. The authors are thankful to Jessica Moniz and Dr. Mary Walker for the tensile test access and assistance at the University of Missouri-Kansas City School of Dentistry.

References

(1) Levental, I.; Georges, P. C.; Janmey, P. A. Soft biological materials and their impact on cell function. Soft Matter 2007, 3, 299–306.

(2) Freutel, M.; Schmidt, H.; Dürselen, L.; Ignatius, A.; Galbusera, F. Finite element modeling of soft tissues: material models, tissue interaction and challenges. Clinical Biomechanics 2014, 29, 363–372.

(3) Xia, T.; Liu, W.; Yang, L. A review of gradient sti!ness hydrogels used in tissue engineering and regenerative medicine. Journal of Biomedical Materials Research Part A 2017, 105, 1799–1812.

(4) Mazzoni, E.; Iaquinta, M. R.; Lanzillotti, C.; Mazziotta, C.; Maritati, M.; Montesi, M.; Sprio, S.; Tampieri, A.; Tognon, M.; Martini, F. Bioactive materials for soft tissue repair. Frontiers in Bioengineering and Biotechnology 2021, 9, 613787.

(5) Jiang, T.; Munguia-Lopez, J. G.; Flores-Torres, S.; Kort-Mascort, J.; Kinsella, J. M. Extrusion bioprinting of soft materials: An emerging technique for biological model fabrication. Applied Physics Reviews 2019, 6.

(6) Zhang, Z.; Wang, B.; Hui, D.; Qiu, J.; Wang, S. 3D bioprinting of soft materials-based regenerative vascular structures and tissues. Composites Part B: Engineering 2017, 123, 279–291.

(7) Vithani, K.; Goyanes, A.; Jannin, V.; Basit, A. W.; Gaisford, S.; Boyd, B. J. An overview of 3D printing technologies for soft materials and potential opportunities for lipid-based drug delivery systems. Pharmaceutical Research 2019, 36, 1–20.

(8) Bonacucina, G.; Cespi, M.; Misici-Falzi, M.; Palmieri, G. F. Colloidal soft matter as drug delivery system. Journal of Pharmaceutical Sciences 2009, 98, 1–42.

(9) Gupta, R.; Muralidhara, H.; Davis, H. Structure and phase behavior of phospholipid-based micelles in nonaqueous media. Langmuir 2001, 17, 5176–5183.

(10) Magri, A.; Petriccione, M.; Cerqueira, M. A.; Gutierrez, T. J. Self-assembled lipids for food applications: A review. Advances in Colloid and Interface Science 2020, 285, 102279.

(11) Sato, K. Crystallization of lipids: Fundamentals and applications in food, cosmetics, and pharmaceuticals; John Wiley & Sons, 2018.

(12) Seol, Y.-J.; Kang, H.-W.; Lee, S. J.; Atala, A.; Yoo, J. J. Bioprinting technology and its applications. European Journal of Cardio-Thoracic Surgery 2014, 46, 342–348.

(13) Honaryar, H.; LaNasa, J. A.; Hickey, R. J.; Shillcock, J. C.; Niroobakhsh, Z. Investigating the morphological transitions in an associative surfactant ternary system. Soft Matter 2022, 18, 2611–2633.

(14) Honaryar, H.; Amirfattahi, S.; Niroobakhsh, Z. Associative Liquid-In-Liquid 3D Printing Techniques for Freeform Fabrication of Soft Matter. Small 2023, 19, 2206524.

(15) Xie, B.; Parkhill, R. L.; Warren, W. L.; Smay, J. E. Direct writing of three-dimensional polymer sca!olds using colloidal gels. Advanced Functional Materials 2006, 16, 1685–1693.

(16) Diba, M.; Koons, G. L.; Bedell, M. L.; Mikos, A. G. 3D printed colloidal biomaterials based on photo-reactive gelatin nanoparticles. Biomaterials 2021, 274, 120871.

(17) Huan, S.; Ajdary, R.; Bai, L.; Klar, V.; Rojas, O. J. Low solids emulsion gels based on nanocellulose for 3D-printing. Biomacromolecules 2018, 20, 635–644.

(18) Jalili, A. R.; Satalov, A.; Nazari, S.; Rahmat Suryanto, B. H.; Sun, J.; Ghasemian, M. B.; Mayyas, M.; Kandjani, A. E.; Sabri, Y. M.; Mayes, E.; others Liquid

crystal-mediated 3D printing process to fabricate nano-ordered layered structures. ACS Applied Materials & Interfaces 2021, 13, 28627–28638.

(19) Mishra, D. K.; Pandey, P. M. E!ects of morphological characteristics on the mechanical behavior of 3D printed ordered pore topological Fe sca!old. Materials Science and Engineering: A 2021, 804, 140759.

(20) Rodriguez-Palomo, A.; Lutz-Bueno, V.; Guizar-Sicairos, M.; Kádár, R.; Andersson, M.; Liebi, M. Nanostructure and anisotropy of 3D printed lyotropic liquid crystals studied by scattering and birefringence imaging. Additive Manufacturing 2021, 47, 102289.

(21) Sheth, R.; Balesh, E. R.; Zhang, Y. S.; Hirsch, J. A.; Khademhosseini, A.; Oklu, R. Three-Dimensional Printing: An Enabling Technology for IR. Journal of Vascular and Interventional Radiology 2016, 27, 859–865.

(22) Gao, Q.; He, Y.; zhong Fu, J.; Liu, A.; Ma, L. Coaxial nozzle-assisted 3D bioprinting with built-in microchannels for nutrients delivery. Biomaterials 2015, 61, 203–215.

(23) Deepak Choudhury, M. W. N., Shivesh Anand The arrival of commercial bioprinters - Towards 3D bioprinting revolution! International Journal of Bioprinting 2018, 4, 139.

(24) Mao, H.; Yang, L.; Zhu, H.; Wu, L.; Ji, P.; Yang, J.; Gu, Z. Recent advances and challenges in materials for 3D bioprinting. Progress in Natural Science: Materials International 2020, 30, 618–634, SI: Biomaterials.

(25) Billiet, T.; Gevaert, E.; De Schryver, T.; Cornelissen, M.; Dubruel, P. The 3D printing of gelatin methacrylamide cell-laden tissue-engineered constructs with high cell viability. Biomaterials 2014, 35, 49–62.

(26) Truby, R. L.; Lewis, J. A. Printing soft matter in three dimensions. Nature 2016, 540, 371–378.

(27) Ozbolat, I. T.; Hospodiuk, M. Current advances and future perspectives in extrusion-based bioprinting. Biomaterials 2016, 76, 321–343.

(28) Hospodiuk, M.; Dey, M.; Sosnoski, D.; Ozbolat, I. T. The bioink: A comprehensive review on bioprintable materials. Biotechnology advances 2017, 35, 217–239.

(29) Fazal, F.; Melchels, F. P.; McCormack, A.; Silva, A. F.; Handley, E.-L.; Mazlan, N. A.; Callanan, A.; Koutsos, V.; Radacsi, N. Fabrication of a Compliant Vascular Graft Using Extrusion Printing and Electrospinning Technique. Advanced Materials Technologies 2024, 2400224.

(30) Sgotti Veiga, J.; Reis Carneiro, M.; Molter, R.; Vinciguerra, M.; Yao, L.; Majidi, C.; Tavakoli, M. Toward Fully Printed Soft Actuators: UV-Assisted Printing of Liquid Crystal Elastomers and Biphasic Liquid Metal Conductors. Advanced Materials Technologies 2023, 8, 2300144.

(31) Davoodi, E.; Sarikhani, E.; Montazerian, H.; Ahadian, S.; Costantini, M.; Swieszkowski, W.; Willerth, S. M.; Walus, K.; Mofidfar, M.; Toyserkani, E.; others Extrusion and microfluidic-based bioprinting to fabricate biomimetic tissues and organs. Advanced Materials Technologies 2020, 5, 1901044.

(32) Corder, R. D.; Chen, Y.-J.; Pibulchinda, P.; Youngblood, J. P.; Ardekani, A. M.; Erk, K. A. Rheology of 3D printable ceramic suspensions: e!ects of non-adsorbing polymer on discontinuous shear thickening. Soft Matter 2023, 19, 882–891.

(33) Liaw, C.-Y.; Pereyra, J.; Abaci, A.; Ji, S.; Guvendiren, M. 4D printing of surface morphing hydrogels. Advanced Materials Technologies 2022, 7, 2101118.

(34) Schwab, A.; Levato, R.; D'Este, M.; Piluso, S.; Eglin, D.; Malda, J. Printability and shape fidelity of bioinks in 3D bioprinting. Chemical Reviews 2020, 120, 11028–11055.

(35) Sears, N. A.; Wilems, T. S.; Gold, K. A.; Lan, Z.; Cereceres, S. N.; Dhavalikar, P. S.; Foudazi, R.; Cosgri!-Hernandez, E. M. Hydrocolloid inks for 3D printing of porous hydrogels. Advanced Materials Technologies 2019, 4, 1800343.

(36) Peak, C. W.; Stein, J.; Gold, K. A.; Gaharwar, A. K. Nanoengineered Colloidal Inks for 3D Bioprinting. Langmuir 2018, 34, 917–925.

(37) Williams, A. H.; Roh, S.; Jacob, A. R.; Stoyanov, S. D.; Hsiao, L.; Velev, O. D. Printable homocomposite hydrogels with synergistically reinforced molecular-colloidal networks. Nature Communications 2021, 12, 2834.

(38) Peak, C. W.; Stein, J.; Gold, K. A.; Gaharwar, A. K. Nanoengineered colloidal inks for 3D bioprinting. Langmuir 2018, 34, 917–925.

(39) Deo, K. A.; Murali, A.; Tronolone, J. J.; Mandrona, C.; Lee, H. P.; Rajput, S.; Hargett, S. E.; Selahi, A.; Sun, Y.; Alge, D. L.; others Granular Biphasic Colloidal Hydrogels for 3D Bioprinting. Advanced Healthcare Materials 2024, 2303810.

(40) Diba, M.; Koons, G. L.; Bedell, M. L.; Mikos, A. G. 3D printed colloidal biomaterials based on photo-reactive gelatin nanoparticles. Biomaterials 2021, 274, 120871.

(41) Dou, Z.; Tang, H.; Chen, K.; Li, D.; Ying, Q.; Mu, Z.; An, C.; Shao, F.; Zhang, Y.; Zhang, Y.; Bai, H.; Zheng, G.; Zhang, L.; Chen, T.; Wang, H. Highly elastic and self-healing nanostructured gelatin/clay colloidal gels with osteogenic capacity for minimally invasive and customized bone regeneration. Biofabrication 2023, 15, 025001.

(42) Jiang, Z.; Diggle, B.; Tan, M. L.; Viktorova, J.; Bennett, C. W.; Connal, L. A. Extrusion 3D printing of polymeric materials with advanced properties. Advanced Science 2020, 7, 2001379.

(43) Joas, S.; Tovar, G. E.; Celik, O.; Bonten, C.; Southan, A. Extrusion-based 3D printing of

poly (ethylene glycol) diacrylate hydrogels containing positively and negatively charged groups. Gels 2018, 4, 69.

(44) Tytgat, L.; Van Damme, L.; Arevalo, M. d. P. O.; Declercq, H.; Thienpont, H.; Otteveare, H.; Blondeel, P.; Dubruel, P.; Van Vlierberghe, S. Extrusion-based 3D printing of photo-crosslinkable gelatin and ϕ-carrageenan hydrogel blends for adipose tissue regeneration. International Journal of Biological Macromolecules 2019, 140, 929–938.

(45) Bom, S.; Ribeiro, R.; Ribeiro, H. M.; Santos, C.; Marto, J. On the progress of hydrogel-based 3D printing: Correlating rheological properties with printing behaviour. International Journal of Pharmaceutics 2022, 615, 121506.

(46) Placone, J. K.; Engler, A. J. Recent advances in extrusion-based 3D printing for biomedical applications. Advanced Healthcare Materials 2018, 7, 1701161.

(47) Bertassoni, L. E.; Cardoso, J. C.; Manoharan, V.; Cristino, A. L.; Bhise, N. S.; Araujo, W. A.; Zorlutuna, P.; Vrana, N. E.; Ghaemmaghami, A. M.; Dokmeci, M. R.; Khademhosseini, A. Direct-write bioprinting of cell-laden methacrylated gelatin hydrogels. Biofabrication 2014, 6, 024105.

(48) Ouyang, L.; Highley, C. B.; Rodell, C. B.; Sun, W.; Burdick, J. A. 3D Printing of Shear-Thinning Hyaluronic Acid Hydrogels with Secondary Cross-Linking. ACS Biomaterials Science & Engineering 2016, 2, 1743–1751.

(49) Abedi, K.; Keshvari, H.; Solati-Hashjin, M. Extrusion-based bioprinting: considerations toward gelatin-alginate bioink. Rapid Prototyping Journal 2024,

(50) Honaryar, H.; Amirfattahi, S.; Nguyen, D.; Kim, K.; Shillcock, J. C.; Niroobakhsh, Z. A Versatile Approach to Stabilize Liquid–Liquid Interfaces using Surfactant Self-Assembly. Small 2024, 2403013.

(51) Amirfattahi, S.; Honaryar, H.; Niroobakhsh, Z. Fabrication of Bijels via Solvent Transfer-Induced Phase Separation using Liquid-in-Liquid Printing. Small Structures 2024, 5, 2300187.

(52) Noirjean, C.; Testard, F.; Jestin, J.; Taché, O.; Dejugnat, C.; Carriere, D. Quenched microemulsions: a new route to proton conductors. Soft Matter 2014, 10, 5928–5935.

(53) Niroobakhsh, Z.; LaNasa, J. A.; Belmonte, A.; Hickey, R. J. Rapid Stabilization of Immiscible Fluids using Nanostructured Interfaces via Surfactant Association. Physical Review Letters 2019, 122, 178003.

(54) Honaryar, H.; LaNasa, J. A.; Lloyd, E. C.; Hickey, R. J.; Niroobakhsh, Z. Fabricating Robust Constructs with Internal Phase Nanostructures via Liquid-in-Liquid 3D Printing. Macromolecular Rapid Communications 2021, 42, 2100445.

(55) Johansson, I.; Svensson, M. Surfactants based on fatty acids and other natural hydrophobes. Current Opinion in Colloid & Interface Science 2001, 6, 178–188.

(56) Katiyar, S. S.; Kushwah, V.; Dora, C. P.; Patil, R. Y.; Jain, S. Design and toxicity evaluation of novel fatty acid-amino acid-based biocompatible surfactants. AAPS PharmSciTech 2019, 20, 186.

(57) Parsana, N.; Kumar, S.; Aswal, V. K.; Seoud, O. E.; Malek, N. I. Self-healable, injectable, and conductive supramolecular eutectogel for the encapsulation and sustained release of the anticancer drug curcumin. ACS Applied Engineering Materials 2022, 1, 380–393.

(58) Burnett, C.; others Safety Assessment of Fatty Acids & Fatty Acid Salts as Used in Cosmetics. Ingredient Review: Washington, DC, USA 2019,

(59) Bercea, M. Rheology as a tool for fine-tuning the properties of printable bioinspired gels. Molecules 2023, 28, 2766.

(60) Amirfattahi, S.; Honaryar, H.; Ghazali, H. s.; Dyke, R.; Reaves, L.; Hurshman, C.; Kim, K.; Kador, K. E.; Niroobakhsh, Z. A nanostructured hydrogel biomaterial system based on lipid and biocompatible oil: From design to its application in liquid-in-liquid 3D printing. Preprint 2025,

(61) Hao, J.; Ho!mann, H. Self-assembled structures in excess and salt-free catanionic surfactant solutions. Current Opinion in Colloid and Interface Science 2004, 9, 279–293.

(62) Fameau, A.-L.; Zemb, T. Self-assembly of fatty acids in the presence of amines and cationic components. Advances in Colloid and Interface Science 2013, 207, 43–64.

(63) Perez-Sanchez, G.; Gomes, J. R. B.; Jorge, M. Modeling Self-Assembly of Silica/Surfactant Mesostructures in the Templated Synthesis of Nanoporous Solids. Langmuir 2013, 29, 2387–2396, PMID: 23343439.

(64) Gillispie, G.; Prim, P.; Copus, J.; Fisher, J.; Mikos, A. G.; Yoo, J. J.; Atala, A.; Lee, S. J. Assessment methodologies for extrusion-based bioink printability. Biofabrication 2020, 12, 022003.

(65) Gillispie, G. J.; Copus, J.; Uzun-Per, M.; Yoo, J. J.; Atala, A.; Niazi, M. K. K.; Lee, S. J. The correlation between rheological properties and extrusion-based printability in bioink artifact quantification. Materials & design 2023, 233, 112237.

(66) Villar, G.; Graham, A. D.; Bayley, H. A tissue-like printed material. Science 2013, 340, 48–52.

(67) Vining, K. H.; Mooney, D. J. Mechanical forces direct stem cell behaviour in development and regeneration. Nature Reviews Molecular Cell Biology 2017, 18, 728–742.

(68) Chaudhuri, O.; Cooper-White, J.; Janmey, P. A.; Mooney, D. J.; Shenoy, V. B. E!ects of extracellular matrix viscoelasticity on cellular behaviour. Nature 2020, 584, 535–546.

(69) Linder-Ganz, E.; Gefen, A. Mechanical compression-induced pressure sores in rat hindlimb: muscle sti!ness, histology, and computational models. Journal of Applied Physiology 2004, 96, 2034–2049.

(70) Wu, Y.; Cazorla, O.; Labeit, D.; Labeit, S.; Granzier, H. Changes in titin and collagen underlie diastolic sti!ness diversity of cardiac muscle. Journal of molecular and cellular cardiology 2000, 32, 2151–2161.

(71) Li, H.; Hao, J. Phase Behavior of Salt-Free Catanionic Surfactant Aqueous Solutions with Fullerene C60 Solubilized. The Journal of Physical Chemistry B 2007, 111, 7719–7724, PMID: 17579395.

(72) Noirjean, C.; Testard, F.; Jestin, J.; Taché, O.; Dejugnat, C.; Carriere, D. Quenched microemulsions: a new route to proton conductors. Soft Matter 2014, 10, 5928–5935.

(73) Noirjean, C.; Testard, F.; Dejugnat, C.; Jestin, J.; Carriere, D. Molten fatty acid based microemulsions. Physical Chemistry Chemical Physics 2016, 18, 15911–15918.